Polarization map of correlated sideband generation in vectorial four-wave mixing

N. L. Petrov, A. A. Voronin, A. B. Fedotov, and A. M. Zheltikov

Citation: Appl. Phys. Lett. **110**, 181108 (2017); doi: 10.1063/1.4982209
View online: http://dx.doi.org/10.1063/1.4982209
View Table of Contents: http://aip.scitation.org/toc/apl/110/18
Published by the American Institute of Physics

APPLIED PHYSICS LETTERS **110**, 181108 (2017)

Polarization map of correlated sideband generation in vectorial four-wave mixing

N. L. Petrov,[1] A. A. Voronin,[1,3,4] A. B. Fedotov,[1,3,4] and A. M. Zheltikov[1,2,3,4]
[1]*Physics Department, International Laser Center, M.V. Lomonosov Moscow State University, Moscow 119992, Russia*
[2]*Department of Physics and Astronomy, Texas A&M University, College Station, Texas 77843, USA*
[3]*Russian Quantum Center, ul. Novaya 100, Skolkovo, Moscow Region 143025, Russia*
[4]*Kazan Quantum Center, A.N. Tupolev Kazan National Research Technical University, Chetaev 18a, 420126 Kazan, Russia*

(Received 29 January 2017; accepted 12 April 2017; published online 2 May 2017)

Polarization analysis of vectorial four-wave mixing (FWM) in birefringent photonic-crystal fibers reveals physically significant tendencies in the behavior of FWM sideband correlations as a function of fiber birefringence, dispersion, and nonlinearity, as well as the pump intensity and bandwidth. Scanning over this parameter space is shown to steer vectorial FWM from largely decoupled sideband generation by individual polarization modes of the pump to FWM scenarios enabling multipartite entanglement generation. *Published by AIP Publishing.*
[http://dx.doi.org/10.1063/1.4982209]

Four-wave mixing (FWM) in optical fibers provides a compact, tunable, and efficient source of correlated photon pairs.[1–4] Modern fiber technologies lend a vast parameter space to tailor the quantum state of such photon pairs,[5,6] helping tune their entanglement degree and enabling the generation of factorable photon states.[7] Specifically, photonic crystal fibers (PCFs),[8] where the dispersion and nonlinearity can be tuned by fiber design engineering,[9] have been shown to enable photon-pair generation within a broad range of pump wavelengths,[1–5,10] offering a unique platform for fiber-based quantum communication and information technologies. Highly birefringent fibers,[11] including specifically designed PCFs,[8] have been found to be instrumental in the generation of polarization-entangled photon pairs, opening the ways toward multipartite entanglement.[12]

Four-wave mixing in optical fibers is especially efficient within the parametric gain band, where a high brightness of the FWM output can be achieved at the moderate level of input laser powers.[15,16] Moreover, high FWM efficiencies are ordinarily achieved within the parametric gain band due to phase matching[15,16]—a condition that also helps avoid undesirable spectral correlations between signal and idler photons, facilitating the generation of a factorable photon-pair FWM output.[7] Parametric gain bands are readily observed as prominent, well-resolved features in the spectrum of laser radiation transmitted through a nonlinear fiber, offering an attractive target and an easy solution for highly efficient FWM-based photon-pair generation.

However, both quantum noise and classical noise are also dramatically enhanced within these parametric gain bands, amplifying unwanted signal–idler correlations in FWM,[17–19] thus limiting the suitability of the photon-pair FWM output for a broad class of applications, including heralded photon detection. To adequately address these problems, appropriate regimes of FWM sideband generation need to be identified through in-depth studies of sideband properties along with the underlying physics within the vast pertinent parameter space. Here, as a step toward fulfilling this program, we identify two important and practically significant regimes of vectorial FWM sideband generation in birefringent PCFs. In the first of these regimes, the central wavelength of a broadband laser pump is tuned close to the wavelength of zero group velocity dispersion (GVD), still in the anomalous dispersion of a highly birefringent fiber, giving rise to FWM sidebands whose frequency Ω_0 is comparable to the pump bandwidth $\Delta\omega$. Uniform spectral fringes are observed in this regime within the entire spectrum of the PCF output, including the pump spectrum and its sidebands, indicating that the FWM sidebands are decoupled from each other and are largely controlled by the individual orthogonal polarization modes of the pump. In the second extreme, the central wavelength of the pump lies in the normal dispersion range, near the zero-GVD wavelength of a moderately birefringent fiber, giving rise to FWM sidebands whose frequency is much larger than the pump bandwidth. In this regime, the interference of polarization modes of the fiber shows up in fringes in the central part of the spectrum but not in the sidebands. With the generation of uncorrelated photon pairs through the Raman process suppressed with an appropriate polarization arrangement, FWM sidebands in this regime can build up from multiphoton vacuum modes, evolving to multipartite entangled quantum states of light.

Experiments were performed with a mode-locked Ti:sapphire laser (Fig. 1), which was adjusted to deliver wavelength- and pulse-width-tunable near-infrared pulses with a central wavelength from 760 to 840 nm and an average power up to 600 mW at a repetition rate of 92 MHz. The output pulse width was varied in our experiments from 50 fs to 5 ps by adjusting the width of an intracavity slit, designed to clip the laser bandwidth $\Delta\omega$. Phase-sensitive pulse characterization of the laser output was performed (Fig. 1) by means of frequency-resolved optical gating (FROG) based on second-harmonic generation (SHG). Experiments were performed with linearly polarized laser pulses, whose polarization vector was rotated with the use of half-wavelength plates. The polarization state of the PCF output was mapped by measuring the

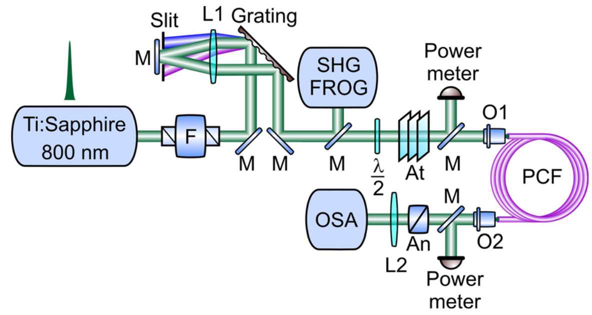

FIG. 1. (a) Experimental setup: M, mirrors; L1 and L2, lenses; At, attenuators; An, polarization analyzer; O1 and O2, objectives; OSA, optical spectrum analyzer; PCF, photonic-crystal fiber; F, Faraday isolator; $\lambda/2$, half-wave plate.

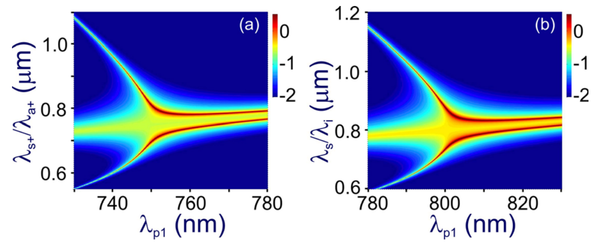

FIG. 2. The coherence length $l_c = \pi/|\Delta\beta|$ for the $2\omega_{p1} = \omega_{s+} + \omega_{a+}$ FWM process as a function of λ_{p1} and $\lambda_{s,a+}$ for the PCFs of the first (a) and second (b) types.

spectra of radiation transmitted through the PCF as a function of the angle α of a polarization analyzer placed behind the fiber (Fig. 1).

Two types of fused silica PCFs were used in experiments. Both the fibers have been fabricated using the standard PCF fabrication technology,[8,14] with their dispersion and nonlinearity tailored by varying the core diameter and the air-filling fraction of the fiber cladding.[8,20] The first PCF had a core diameter $d \approx 1.8\,\mu$m, an effective mode-field diameter $\rho \approx 1.6\,\mu$m, a numerical aperture NA ≈ 0.38, a nonlinearity coefficient $\gamma \approx 0.10\,\mathrm{W^{-1}m^{-1}}$, and a zero-GVD wavelength $\lambda_z \approx 750$ nm. The second fiber had a core diameter $d \approx 2.3\,\mu$m, $\rho \approx 1.9\,\mu$m, NA ≈ 0.22, $\gamma \approx 0.07\,\mathrm{W^{-1}m^{-1}}$, and $\lambda_z \approx 800$ nm. Both the fibers exhibit noticeable birefringence, facilitating the studies of FWM sideband generation in orthogonal polarization modes. Experiments presented in this paper were performed with a 0.5-m stretch of the first fiber and a 1.8-m segment of the second-type PCF.

For efficient laser-beam–fiber coupling, the Ti:sapphire-laser output is focused with a 40×, 0.65-NA Olympus Plan Achromat microscope objective, providing beam-waist diameters of ≈1.5-μm and ≈1.6-μm at wavelengths of 750 and 800 nm, respectively, thus corresponding to 88% and 71% of the effective fiber mode area in experiments with PCFs of the first and second types. The polarized Ti:sapphire-laser output is launched into a PCF at a fixed angle φ with respect to the fast-mode fiber axis, giving rise to two orthogonally polarized fields with close central frequencies ω_{p1} and ω_{2p} coupled into the fast and slow polarization modes of the fiber. These fields serve as a pump in FWM processes, giving rise to Stokes and anti-Stokes sidebands with central frequencies $\omega_{s\pm}$ and $\omega_{a\pm}$ in the fast (+) and slow (–) polarization modes of the fiber. The parametric gain in each of the FWM processes contributing to sideband generation is controlled by the mismatch $\Delta\beta$ between the propagation constants β_{p1}, β_{p2}, $\beta_{s\pm}$, and $\beta_{a\pm}$ of the fields involved in the FWM process.

In Figs. 2(a) and 2(b), we plot the coherence length $l_c = \pi/|\Delta\beta|$ for one of such FWM processes, $2\omega_{p1} = \omega_{s+} + \omega_{a+}$, as a function of $\lambda_{p1} = 2\pi c/\omega_{p1}$ and $\lambda_{s,a+} = 2\pi c/\omega_{s,a+}$ for the first and second PCFs studied in our experiments. As can be seen from these maps, when used with a wavelength-tunable, 760–840-nm laser pump, this pair of fibers with close zero-GVD wavelengths enables a systematic study of FWM sideband generation in orthogonal polarization modes as a function of fiber dispersion, as well as the $\Delta\omega/\Omega_0$ ratio, with $\Omega_0 = \omega_{a\pm} - \omega_{p1,p2} = \omega_{p1,p2} - \omega_{s\pm}$ being the central frequency of the FWM parametric gain band.

As an important general tendency, recognized in the extensive earlier literature,[21–23] the FWM phase-matching maps and, hence, the maps of the FWM gain look drastically different for the normal and anomalous GVD regions (Figs. 2(a) and 2(b)). When the wavelength of the pump with a peak power P_0 lies in the region of anomalous dispersion, where $\beta_2 = \partial^2\beta/\partial\omega^2 < 0$, a simple $\beta_2\Omega_0^2 + 2\gamma P_0 = 0$ phase matching is possible for parametric FWM processes, giving rise to two phase-matching branches with the center of the FWM parametric gain band separated from ω_p by just $\Omega_0 = (2\gamma P_0/|\beta_2|)^{1/2}$.

In the region of normal dispersion, on the other hand, the $\beta_2\Omega_0^2 + 2\gamma P_0 = 0$ equation has no solutions within the class of real Ω_0 as $\beta_2 > 0$. In this regime, phase matching for the considered class of FWM processes is still possible due to high-order dispersion, giving rise to two phase-matching branches that lie much further away from ω_p. This type of phase matching is observed for $\lambda_{p1} < 750$ nm in Fig. 2(a) and $\lambda_{p1} < 800$ nm in Fig. 2(b).

Since in the regime of normal dispersion, the spectral gap Ω_0 between the central frequency of the pump ω_p and the center of the FWM parametric gain band is much larger than typical Ω_0 values in the anomalous-dispersion region, the first and second PCFs help engineer radically different types of input photon fields $|\psi(z=0)\rangle$ for FWM sideband generation. With the central wavelength of the pump field $\lambda_p > 760$ nm, sideband generation in PCFs of the first class occurs in the regime of anomalous dispersion. Because the sideband frequency in this regime is comparable to or even smaller than the pump bandwidth $\Delta\omega$, increased by Kerr-effect-induced spectral broadening, a broadband laser pump provides a large number of photons n_{ph} at the sideband frequencies $\omega_p \pm \Omega_0$, thus serving as a source of largely classical input fields for FWM sideband generation. Moreover, when the peak power of the laser output is high enough, both the orthogonally polarized modes of the laser pump undergo efficient spectral broadening as they propagate through the fiber, filling the gap between the central part of the spectrum and $\omega_p \pm \Omega_0$ sidebands.

In Figs. 3(a) and 3(b), we present the spectra of the FWM output of the first-type PCF with the Ti:sapphire laser pump coupled into a mixture of polarization modes of the fiber. With the polarization analyzer oriented along one of the polarization modes of the fiber, $\alpha = 190°$ or 280°, pure polarization states of the FWM output, prepared in the orthogonal polarization modes of the fiber, are selected,

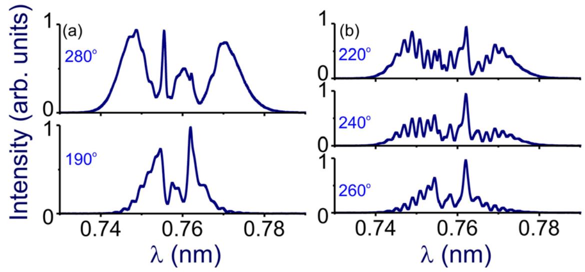

FIG. 3. The spectra of the FWM output of the first-type PCF pumped by Ti:sapphire laser pulses: (a) pure polarization states of the FWM output are selected with the polarization analyzer oriented along one of the polarization modes of the fiber, $\alpha = 190°$ (lower panel) and 280° (upper panel) and (b) a mixture of polarization states of the FWM output is selected with $\alpha = 220°$ (upper panel), 240° (middle panel), and 260° (lower panel).

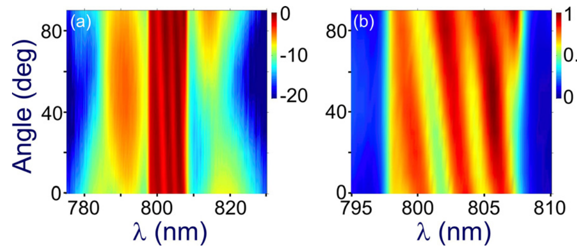

FIG. 5. Polarization maps of the FWM output of the second-type PCF pumped by a spectrally clipped, $\Delta\lambda \approx 5$ nm output of the Ti:sapphire laser: (a) the entire spectrum of the FWM output and (b) close-up of the central part of the PCF output spectrum, featuring clearly resolved fringes.

giving rise to virtually no spectral fringes in the detected FWM (Fig. 3(a)). When, on the other hand, the polarization analyzer is oriented in such a way so as to select a mixture of polarization states, clearly resolved fringes are observed in the detected FWM spectra. These fringes, resulting from the spectral interference of the FWM-coupled pump and sidebands in the two orthogonally polarized modes of the fiber,[24] are remarkably uniform across the entire output spectrum. In Fig. 3(b), the spacing of these fringes, $\delta\lambda \approx 2$ nm, remains unchanged within the entire bandwidth of the fiber output, covering the central part, corresponding to the spectrally broadened pump, and its sidebands. For a fiber stretch with a length $L = 50$ cm, this spacing is $\delta\lambda \approx 2$ nm, which corresponds to a birefringence $\delta n \approx 6 \times 10^{-4}$.

The fibers of the second type provide normal dispersion for a laser pump with $\lambda_p < \lambda_z$, providing much larger separations between the FWM sidebands and the pump (Fig. 2(b)), thus helping prevent the seeding of FWM sideband generation by a broadband pump. Since the Kerr effect can still broaden the pump to such an extent that it starts to seed sideband generation (cf. Figs. 4(a) and 4(b)), the laser bandwidth was reduced in our experiments to $\Delta\lambda \approx 5$, for a better isolation of the FWM sidebands from the pump, by adjusting a slit inside the laser cavity (Fig. 1).

In Fig. 5(a), we present a typical polarization map of FWM sideband generation in second-type PCF pumped by a spectrally clipped, $\Delta\lambda \approx 5$ nm output of the Ti:sapphire laser. The polarization state of the PCF output in these experiments is mapped by measuring the spectra of radiation transmitted through the PCF as a function of the angle α of the polarization analyzer. Similar to the FWM output of the PCF of the first type, the interference of polarization modes of the fiber shows up in high-visibility fringes in the central part of the spectrum (Fig. 5(b)). The phase of these fringes is seen to follow the variations of the analyzer angle α. The polarization properties of the sidebands are, however, strikingly different. While the FWM sidebands generated in the PCF of the first type exhibit well-resolved polarization fringes whose period and phase are the same as those of the central part of the spectrum (Fig. 3(b)), the sidebands delivered by the second-type PCF display no sign of fringes whatsoever (Fig. 5(a)). This regime of FWM is of special interest for the generation of a variety of quantum states of light. In particular, when the input state of the laser field is a two-mode vacuum state, the FWM-sideband output is in the squeezed state.[12,13] On the other hand, when the input photon field is in a four-mode vacuum state, this regime of FWM sideband generation enables a multipartite entanglement.[12,13,25]

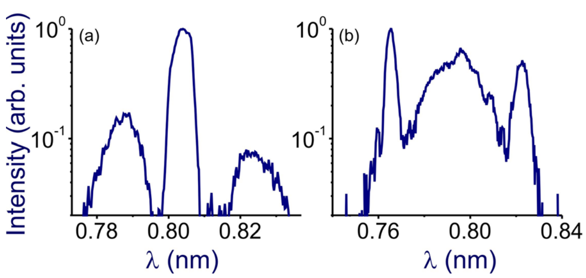

FIG. 4. The spectra of the FWM output of the second-type PCF pumped by Ti:sapphire laser pulses with $\Delta\lambda \approx 5$ nm (a) and 15 nm (b).

While the general tendencies of FWM sideband generation in PCFs have been identified in the earlier work,[1–4,26–29] the main focus of this work is to understand the properties of correlated photon pairs generated through a vectorial, polarization-controlled FWM. To this end, we study vectorial FWM sideband generation in birefringent PCFs as a function of fiber birefringence, dispersion, and nonlinearity, as well as the pump intensity and bandwidth. Scanning over this parameter space has been shown to steer vectorial FWM from largely decoupled sideband generation by individual polarization modes of the pump to FWM scenarios enabling multipartite entanglement generation. Moreover, our experiments demonstrate a high efficiency of cross-polarized FWM sideband generation (Figs. 5(a) and 5(b)), that is, in an arrangement where the polarization of FWM sidebands is orthogonal to the polarization of the pump field, thus allowing an efficient suppression of uncorrelated photon generation through the Raman scattering process.[19] Specifically, for FWM sidebands with $\Omega_0 \approx 9$ THz, as those shown in Figs. 4(a) and 5(a), the photon-pair correlation coefficient η is about 8 for FWM sidebands copolarized with the pump, limited by the Raman effect, which gives rise to uncorrelated Stokes and anti-Stokes photon pairs. For FWM sidebands cross-polarized with the pump field, on the other hand, the generation of uncorrelated photons through the Raman process is efficiently suppressed,[19] providing much higher photon-pair correlation coefficients, $\eta \approx 45$ at $\Omega_0 \approx 9$ THz.

The efficiency of FWM sideband generation can be varied in these experiments within a broad range by changing the pump power and polarization geometry, yielding an FWM sideband output ranging from the single-photon up to the milliwatt level of average powers. Specifically, for the conditions of experiments presented in Figs. 3–5, the average powers of Stokes/anti-Stokes sidebands are 0.7/0.7 mW and 0.7/0.8 mW in the upper and lower plots in Fig. 3(a), 0.4/1.0 mW, 0.5/0.8 mW, and 0.7/0.7 mW in the upper, middle, and lower plots in Fig. 3(b), 0.08/0.1 mW in Fig. 4(a), and 0.09/0.14 mW in Fig. 4(b). The corresponding FWM sideband output field intensities are 0.5/0.5 GW/cm^2 and 0.5/0.6 GW/cm^2 in the upper and lower plots in Fig. 3(a), 0.3/0.8 GW/cm^2, 0.3/0.6 GW/cm^2, and 0.5/0.6 GW/cm^2 in the upper, middle, and lower plots in Fig. 3(b), 0.1/0.2 GW/cm^2 in Fig. 4(a), and 0.05/0.08 GW/cm^2 in Fig. 4(b). In Fig. 5, as the angle α of the polarization analyzer varies from 0 to $\pi/4$, the average powers of the FWM sidebands at the fiber output change from 0.07 to 0.03 mW for the Stokes signal and from 0.07 to 0.10 mW for the anti-Stokes sideband. The corresponding output field intensities vary from 0.12 to 0.06 GW/cm^2 for the Stokes sideband and from 0.12 to 0.17 GW/cm^2 for the anti-Stokes field.

The results of experiments presented in this paper lead us to identify two important and practically significant regimes of vectorial FWM sideband generation in birefringent PCFs. In the first of these regimes, the central wavelength of a broadband laser pump is tuned close to the zero-GVD wavelength in the anomalous dispersion of a highly birefringent fiber, giving rise to FWM sidebands whose central frequency is comparable to the pump bandwidth. Uniform spectral fringes are observed in this regime within the entire spectrum of the PCF output, including the pump spectrum and its sidebands, indicating that the FWM sidebands are decoupled from each other and are largely controlled by the individual orthogonal polarization modes of the pump. In the second extreme, the central wavelength of the pump lies in the normal dispersion range, near the zero-GVD wavelength of a moderately birefringent fiber, giving rise to FWM sidebands whose frequency is much larger than the pump bandwidth. In this regime, the interference of polarization modes of the fiber shows up in fringes in the central part of the spectrum but not in the sidebands. With the generation of uncorrelated photon pairs through the Raman process suppressed with an appropriate polarization arrangement, FWM sidebands in this regime can build up from multiphoton vacuum modes, evolving to multipartite entangled quantum states of light.

Stimulating discussions with A. A. Kalachev and S. I. Moiseev are gratefully acknowledged. Research into waveguide systems for quantum technologies has been supported by the Government of Russian Federation (Project No. 14.Z50.31.0040, Feb. 17, 2017).

[1]J. E. Sharping, J. Chen, X. Li, P. Kumar, and R. S. Windeler, Opt. Express **12**, 3086 (2004).
[2]J. G. Rarity, J. Fulconis, J. Duligall, W. J. Wadsworth, and P. St. J. Russell, Opt. Express **13**, 534 (2005).
[3]J. Fulconis, O. Alibart, W. J. Wadsworth, P. St. J. Russell, and J. G. Rarity, Opt. Express **13**, 7572 (2005).
[4]J. Fulconis, O. Alibart, J. L. O'Brien, W. J. Wadsworth, and J. G. Rarity, Phys. Rev. Lett. **99**, 120501 (2007).
[5]O. Cohen, J. S. Lundeen, B. J. Smith, G. Puentes, P. J. Mosley, and I. A. Walmsley, Phys. Rev. Lett. **102**, 123603 (2009).
[6]M. Medic, J. B. Altepeter, M. A. Hall, M. Patel, and P. Kumar, Opt. Lett. **35**, 802 (2010).
[7]K. Garay-Palmett, H. J. McGuinness, O. Cohen, J. S. Lundeen, R. Rangel-Rojo, A. B. U'Ren, M. G. Raymer, C. J. McKinstrie, S. Radic, and I. A. Walmsley, Opt. Express **15**, 14870 (2007).
[8]P. Russell, Science **299**, 358 (2003).
[9]W. H. Reeves, D. V. Skryabin, F. Biancalana, J. C. Knight, P. St. J. Russell, F. G. Omenetto, A. Efimov, and A. J. Taylor, Nature **424**, 511 (2003).
[10]A. M. Apetrei, J. M. Moison, J. A. Levenson, M. Foroni, F. Poli, A. Cucinotta, S. Selleri, M. Legré, M. Wegmüller, N. Gisin, K. V. Dukel'skii, A. V. Khokhlov, V. S. Shevandin, Yu. N. Kondrat'ev, C. Sibilia, E. E. Serebryannikov, and A. M. Zheltikov, Appl. Phys. B **81**, 409 (2005).
[11]X. Li, P. L. Voss, J. E. Sharping, and P. Kumar, Phys. Rev. Lett. **94**, 053601 (2005).
[12]C. J. McKinstrie, S. J. van Enk, M. G. Raymer, and S. Radic, Opt. Express **16**, 2720 (2008).
[13]C. J. McKinstrie, J. D. Harvey, S. Radic, and M. G. Raymer, Opt. Express **13**, 9131 (2005).
[14]A. M. Zheltikov, Phys. Usp. **43**, 1125 (2000).
[15]R. H. Stolen and J. E. Bjorkholm, IEEE J. Quantum Electron. **18**, 1062 (1982).
[16]G. P. Agrawal, *Nonlinear Fiber Optics*, 4th ed. (Elsevier, 2007).
[17]C. J. McKinstrie, S. Radic, and M. G. Raymer, Opt. Express **12**, 5037 (2004).
[18]Q. Lin, F. Yaman, and G. P. Agrawal, Opt. Lett. **31**, 1286 (2006).
[19]Q. Lin, F. Yaman, and G. P. Agrawal, Phys. Rev. A **75**, 023803 (2007).
[20]A. M. Zheltikov, Phys. Usp. **47**, 69 (2004).
[21]J. D. Harvey, R. Leonhardt, S. Coen, G. K. L. Wong, J. C. Knight, W. J. Wadsworth, and P. St. J. Russell, Opt. Lett. **28**, 2225 (2003).
[22]J. M. Dudley, G. Genty, and S. Coen, Rev. Mod. Phys. **78**, 1135 (2006).
[23]A. M. Zheltikov, Phys. Usp. **49**, 605 (2006).
[24]A. A. Voronin, I. V. Fedotov, J. Kobelke, M. Jäger, K. Schuster, A. B. Fedotov, H. Bartelt, and A. M. Zheltikov, Opt. Lett. **37**, 5163 (2012).
[25]A. M. Zheltikov, "Phase matching as a gate for photon entanglement," Sci. Rep. (to be published).
[26]A. Ling, J. Chen, J. Fan, and A. Migdall, Opt. Express **17**, 21302 (2009).
[27]S. Coen, A. H. L. Chau, R. Leonhardt, J. D. Harvey, J. C. Knight, W. J. Wadsworth, and P. S. J. Russell, J. Opt. Soc. Am. B **19**, 753 (2002).
[28]Y. Li, J. Hou, Z. Jiang, and J. Leng, Appl. Opt. **52**, 2049–2054 (2013).
[29]Y. Li, J. Hou, Z. Jiang, J. Leng, and L. Huang, J. Opt. **16**, 025202 (2014).